Natural Resources for Human Health
eISSN: 2583-1194

Original Research

Received 20 July 2026
Revised 27 Aug 2026
Accepted 15 Sep 2026

Natural Resources for Human Health 2026, Vol. 6 (20s): 1015–1031

KEYWORDS:
phloridzin; dipeptidyl peptidase-IV; molecular docking; molecular dynamics simulation; MM-GBSA; type 2 diabetes mellitus; dihydrochalcone

Integrated In Silico and In Vitro Evaluation of Phloridzin for Dipeptidyl Peptidase-IV Inhibition and Glucose Uptake in Type 2 Diabetes Mellitus

Vaishnavi Munnangi[1], Patel Dhruv Jatinkumar[1], Krishna Shevate[2], Kalirajan Rajagopal[2], Vadivelan Ramachandran[1]*

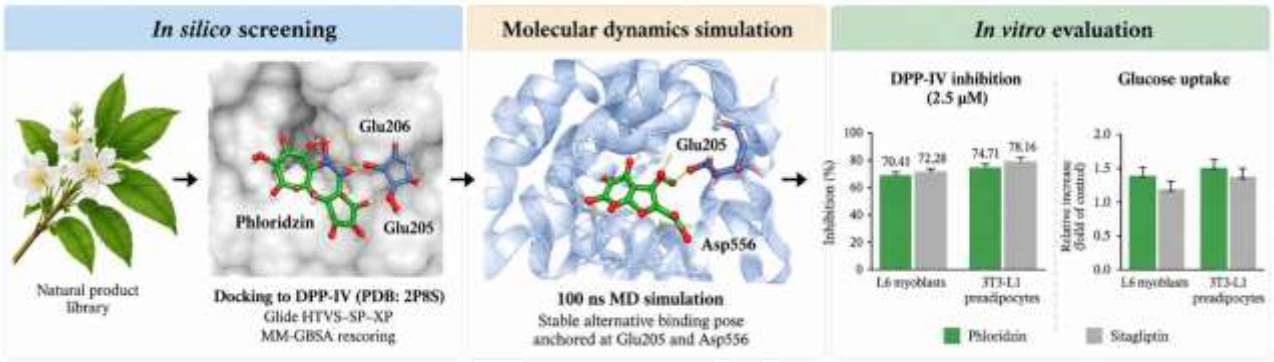
[1]Department of Pharmacology, JSS College of Pharmacy, JSS Academy of Higher Education & Research, Ooty, Nilgiris, Tamil Nadu, India – 643001.
[2]Department of Pharmaceutical Chemistry, JSS College of Pharmacy, JSS Academy of Higher Education & Research, Ooty, Nilgiris, Tamil Nadu, India – 643001.
Corresponding Author: Vadivelan Ramachandran
Email: vadivelanr@jssuni.edu.in
ORCID ID: 0000-0001-7927-4554
Co-Authors
Vaishnavi Munnangi
ORCID ID: 0009-0006-3328-9121
Patel Dhruv Jatinkumar
ORCID ID: 0009-0003-9780-3300
Krishna Shevate
ORCID ID:0000-0001-6314-8641
Kalirajan Rajagopal
ORCID ID: 0000-0003-3382-4316

ABSTRACT: Dipeptidyl peptidase-IV (DPP-IV, CD26) inactivates the incretin hormones and several peptide mediators of tissue repair, and its pharmacological inhibition is an established strategy in type 2 diabetes mellitus. Plant-derived polyphenols are an attractive source of DPP-IV inhibitors, but few candidates have been carried from structure-based screening through to cell-based enzyme assays within a single study. In the present work a natural-product library was screened against the DPP-IV crystal structure 2P8S using a hierarchical Glide HTVS–SP–XP workflow, the highest-ranked poses were rescored by Prime MM-GBSA, and the leading compound was followed through a 100 ns Desmond molecular dynamics simulation. That compound was then evaluated experimentally in rat L6 myoblasts and mouse 3T3-L1 preadipocytes: for cytotoxicity by sulforhodamine B assay, for glucose uptake by the glucose oxidase–peroxidase method, and for DPP-IV inhibition by a chromogenic H-Gly-Pro-p-nitroanilide assay in both cell-free and cell-lysate formats, with sitagliptin as the reference inhibitor. Phloridzin ranked highest in extra-precision docking (Glide g-score −9.821 kcal/mol) and in MM-GBSA rescoring (ΔGbind −79.494 kcal/mol), ahead of the co-crystallised sitagliptin analogue (−8.384 and −20.289 kcal/mol, respectively), its advantage arising from hydrogen bonding (XP HBond −5.201 kcal/mol) and electrostatics (ΔGcoul −100.76 kcal/mol) at the canonical Glu205/Glu206 motif of the S2 subsite. Over 100 ns the protein Cα RMSD remained between 1.5 and 2.5 Å and ligand-contacting residues fluctuated below approximately 1 Å, but the ligand left its docked pose within the first 25 ns and thereafter occupied a stable alternative pose,

Natural Resources for Human Health
eISSN: 2583-1194

maintaining hydrogen bonds to Glu205 (50% and 35% occupancy) and Asp556 (46%). Phloridzin inhibited DPP-IV concentration-dependently in both cell systems, reaching 70.41 ± 0.74% inhibition in L6 and 74.71 ± 1.75% in 3T3-L1 cells at 2.5 μM against 72.28 ± 2.45% and 78.16 ± 1.41% for sitagliptin. Glucose uptake increased in both lines. Phloridzin is therefore a credible natural DPP-IV inhibitor whose computationally predicted affinity is borne out functionally; the simulation indicates that its stable complex is a rearranged pose anchored at Glu205 and Asp556 rather than the docked pose, a distinction relevant to any future optimization of dihydrochalcone scaffolds.

Graphical Abstract:



1. INTRODUCTION

Type 2 diabetes mellitus is sustained by the progressive failure of insulin secretion to match insulin demand, and much of the therapeutic effort of the past two decades has been directed at the incretin axis that couples nutrient intake to insulin release. Glucagon-like peptide-1 and glucose-dependent insulinotropic polypeptide are released from the intestine after a meal and potentiate glucose-stimulated insulin secretion, but both are cleaved within minutes by dipeptidyl peptidase-IV (DPP-IV, also designated CD26), a serine exopeptidase that removes N-terminal dipeptides from substrates carrying proline or alanine in the penultimate position. Inhibiting that cleavage prolongs incretin action and lowers glycaemia without directly stimulating insulin release, which is the pharmacological basis of the gliptin class [1]. The crystallographic architecture of the enzyme is well characterized: a catalytic triad sits at the base of a large internal cavity reached through a side opening and a propeller channel, with the S1 pocket conferring the preference for proline or alanine and the adjacent S2 subsite presenting a pair of glutamate residues, Glu205 and Glu206, that anchor the free N-terminus of a substrate or an amine-bearing inhibitor [2].

The biological reach of DPP-IV extends well beyond the incretins. Its expression changes markedly in inflammation, obesity, cancer and diabetes, and its substrate repertoire includes mediators that are central to tissue repair, among them stromal cell-derived factor-1 (SDF-1), insulin-like growth factor-1 (IGF-1) and vascular endothelial growth factor [1]. SDF-1 signaling recruits haematopoietic and endothelial progenitor cells to ischaemic tissue, while IGF-1 drives keratinocyte and fibroblast proliferation and granulation-tissue formation in animal models of repair [3]. DPP-IV activity is itself sensitive to the diabetic milieu: endothelial cells exposed to high glucose display elevated DPP-IV activity [4], and advanced glycation end-products stimulate release of soluble DPP-IV, whose interaction with the mannose 6-phosphate/IGF-II receptor increases endothelial reactive oxygen species production [5]. Genetic analyses have also linked the *DPP4* locus to cardiovascular risk factors in obesity [6]. These observations place DPP-IV at the intersection of glycaemic control, vascular inflammation and impaired healing, and they explain the continuing interest in new chemical matter directed at the enzyme.

Hyperglycaemia impairs repair through a partly overlapping set of mechanisms. Sustained high glucose suppresses angiogenic growth factors including fibroblast growth factor 2, SDF-1 and vascular endothelial growth factor A, compromising endothelial function, prolonging the inflammatory phase and limiting angiogenesis, with hypoxia and delayed closure as the consequences [7]. The clinical expression of this physiology is substantial: between 9.1 and 26.1 million diabetic foot ulcers are estimated to occur worldwide each year [8], and 15 to 25% of people with diabetes will develop one during their lifetime [9]. Deep-tissue sampling studies underline how difficult these lesions are to characterize and manage reliably [9].

Natural Resources for Human Health
eISSN: 2583-1194

Against this background, plant-derived polyphenols have attracted attention as a source of DPP-IV inhibitors with favorable safety profiles. Phloridzin (phloretin 2'-O-β-D-glucopyranoside) is the principal dihydrochalcone of apple bark, core and peel and is distributed widely in the genus *Malus* [10]. It is historically important as the compound from which sodium–glucose cotransporter pharmacology was derived, and it carries documented anti-inflammatory, antioxidant, antimicrobial and antidiabetic activity [10]. Its structure (Figure 1) combines a glucose unit with a dihydrochalcone bearing four phenolic hydroxyl groups, giving eight hydrogen-bond donors distributed across two conformationally independent regions of the molecule - a feature that proves central to the binding behavior described below.

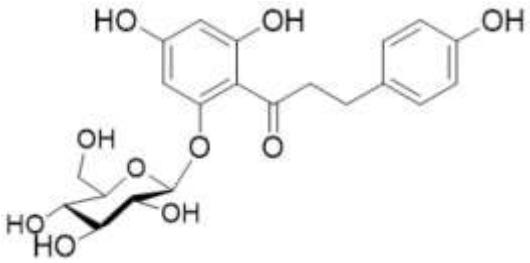


Figure 1. Structure of phloridzin (phloretin 2'-O-β-D-glucopyranoside), PubChem CID 6072.

Independent docking work has already suggested that phlorizin (a synonym of phloridzin) binds the DPP-IV structure 2P8S with a predicted affinity exceeding that of sitagliptin [11], and phenolic compounds more generally have been shown to potentiate hypoglycaemia through DPP-IV inhibition [12]. What has been lacking is a study that screens a natural-product library against DPP-IV without presupposing the answer, interrogates the stability of the resulting complex over a meaningful simulation timescale, and then tests the prioritized compound experimentally in cells rather than stopping at the computational prediction.

The present work was designed to close that gap. A natural-product library was screened against the DPP-IV active site by a hierarchical docking workflow, the highest-ranked compounds were rescored by MM-GBSA, and the leading candidate was followed through a 100 ns molecular dynamics simulation to establish whether the docked pose survives thermal motion. The prioritized compound was then evaluated in rat L6 myoblasts and mouse 3T3-L1 preadipocytes for cytotoxicity, glucose uptake and DPP-IV inhibition, with sitagliptin as the reference inhibitor. The objective was neither to demonstrate superiority over an established drug nor to propose a formulation, but to establish whether a structure-based prediction for a widely available dihydrochalcone is reproduced in a cellular setting, and to describe the binding behaviors accurately enough to be useful to subsequent medicinal-chemistry work.

2. MATERIALS AND METHODS

2.1 Software and structure preparation

All computational work was performed with the Schrödinger Suite, Maestro version 14.0. Docking, rescoring and ligand preparation used release 2024-2; the molecular dynamics production run used release 2024-1. The crystal structure of DPP-IV in complex with the sitagliptin analogue 417 cyclohexylamine (PDB ID: 2P8S) was retrieved from the RCSB Protein Data Bank [13] and prepared with the Protein Preparation Wizard. Bond orders were assigned, hydrogen atoms were added, heteroatom states were reassigned and water molecules were removed with the exception of those conserved at the interaction interface. Hydroxyl group orientations, histidine tautomers and protonation states, and the amide flips of asparagine and glutamine side chains were optimized, and assignments were checked by visual inspection. The prepared structure was then energy-minimized with the OPLS-4 force field to relieve steric strain [14].

A receptor grid was generated with the Glide grid-generation wizard, centered on the centroid of the co-crystallized ligand, with grid box dimensions of 14 Å × 14 Å × 14 Å.

2.2 Ligand library preparation

A library of natural-product structures obtained from the COCONUT (Collection of Open Natural Products) database [15] was processed with the LigPrep module. Two-dimensional structures were converted to three dimensions with assignment of

stereochemistry, generation of ionization and tautomeric states at pH 7.0 using Epik, desalting, correction of chiralities, addition of missing hydrogens and geometry optimization, followed by energy minimization with the OPLS-4 force field [16].

2.3 Molecular docking

A hierarchical virtual screening protocol was applied with the Glide module. The prepared library was first filtered by High-Throughput Virtual Screening to remove compounds with unpromising predicted binding. Surviving hits were redocked in Standard Precision mode, and the 50 highest-ranked compounds were then docked in Extra Precision (XP) mode. All calculations used the OPLS-4 force field in flexible docking mode, in which conformers are generated for each input ligand during docking. The scoring function rewards favorable lipophilic contact, hydrogen bonding and metal ligation and penalizes steric clashes; final poses were rescored with the Glide Score function [17,18]. Results are reported as the Glide g-score together with the XP hydrogen-bonding term, the Glide van der Waals energy and the total Glide energy, and are compared throughout with the co-crystallized ligand 417 cyclohexylamine redocked under identical conditions.

2.4 Binding free energy calculation

Relative binding free energies for the XP-docked poses were estimated with Prime MM-GBSA. Molecular mechanics energies were computed with the OPLS-4 force field [19] and solvation was treated with the VSGB 2.0 generalized Born/surface area continuum model [20,21]. The total binding free energy (ΔG_{bind}) is reported together with its Coulombic, covalent, hydrogen-bonding, lipophilic and van der Waals components. These values are relative estimates intended for ranking congeneric and non-congeneric poses within a single receptor and are not absolute affinities.

2.5 Molecular dynamics simulation

The top-ranked docked complex was subjected to molecular dynamics simulation with the Desmond module. The complex was solvated in explicit TIP3P water within an orthorhombic cell extending at least 10 Å beyond the solute in each direction, and the system was neutralized with counterions at physiological ionic strength using the OPLS-4 force field. After energy minimization and equilibration under the default Desmond relaxation protocol, a 100 ns production run was performed in the isothermal–isobaric (NPT) ensemble at 300 K and 1.01325 bar, with temperature and pressure controlled by the Nosé–Hoover chain thermostat and the Martyna–Tobias–Klein barostat respectively [22]. Trajectory analysis [23] comprised the root mean square deviation (RMSD) of protein Cα atoms and of the ligand fitted on the protein, the per-residue root mean square fluctuation (RMSF), the protein–ligand contact profile and its persistence over the trajectory, and the ligand property descriptors radius of gyration, intramolecular hydrogen bonds, molecular surface area, solvent-accessible surface area and polar surface area.

2.6 Cell lines and culture

The two cell lines used are characterized in Table 1. Both were obtained from the National Centre for Cell Science, Pune, India.

Table 1. Characteristics of the cell lines used.

Property	L6	3T3-L1
Morphology	Fibroblastoid	Fibroblastoid
Tissue of origin	Skeletal muscle	Whole embryo
Species	Rat	Mouse (Swiss)
Developmental stage	Embryonic	Embryonic
Ploidy	Not stated	Aneuploid
Distinguishing characteristics	Forms myotubes	Contact-inhibited; readily transformed

Stock cultures were maintained in Dulbecco's Modified Eagle Medium supplemented with 10% inactivated fetal bovine serum, penicillin 100 IU/mL, streptomycin 100 µg/mL and amphotericin B 5 µg/mL in a humidified atmosphere of 5% CO_2

at 37 °C until confluent. Cells were dissociated with 0.2% trypsin and 0.02% EDTA in phosphate-buffered saline. Cultures were propagated in 25 cm² flasks; cytotoxicity experiments were performed in 96-well microtitre plates. 3T3-L1 cells were used in the undifferentiated preadipocyte state and were not subjected to an adipogenic differentiation protocol in this study; this line is an established model for the effects of plant-derived compounds on adipocyte metabolism [24].

2.7 Cytotoxicity: sulforhodamine B assay

Cells in exponential growth were washed, trypsinised and resuspended in complete medium, plated at 10,000 cells per well in 96-well plates and incubated for 24 h to allow formation of a partial monolayer. Cells were then exposed to a range of phloridzin concentrations in quadruplicate; control wells received maintenance medium only. Plates were incubated at 37 °C in 5% CO_2 for 72 h, and morphological changes in treated cells were examined by inverted microscopy at intervals and compared with controls.

At 72 h, 50 µL of 50% trichloroacetic acid was layered gently over the medium to give a final concentration of 10%, and plates were held at 4 °C for 1 h. Plates were flicked, washed five times with tap water to remove medium, drug and serum, and air-dried. Fixed cells were stained with sulforhodamine B for 30 min, unbound dye was removed by four rapid washes with 1% acetic acid, and plates were air-dried. Bound dye was solubilized in 100 µL of 10 mM Tris base with vigorous shaking for 5 min, and absorbance was read at 540 nm on a microplate reader. Sulforhodamine B binds basic amino acid residues of trichloroacetic acid-fixed cellular protein under mildly acidic conditions and provides an index of total cellular protein that is linear over at least two orders of magnitude of cell density [25,26].

Growth inhibition was calculated as:

% Growth inhibition = 100 − (mean OD of test group / mean OD of control) × 100

2.8 Glucose uptake assay

Cells were seeded in 24-well plates and incubated for 48 h at 37 °C in 5% CO_2. On formation of a semi-confluent monolayer the medium was replaced with serum-free DMEM containing 0.2% bovine serum albumin and cells were incubated for a further 18 h. The medium was then discarded, cells were washed once with Krebs–Ringer phosphate buffer, and treated with insulin as the reference, phloridzin, and glucose (1 M), then incubated at 37 °C for 30 min. Cells were lysed by three freeze–thaw cycles and the lysate was collected. Glucose uptake was calculated as the difference between initial and final glucose content of the incubation medium, determined by the glucose oxidase–peroxidase method [27].

2.9 DPP-IV inhibition assays

Two complementary assay formats were used. Chromogenic enzyme-inhibition assays of this type are well established for the evaluation of plant-derived antidiabetic agents [28].

Cell-free enzyme assay. Test compound or vehicle was pre-incubated in triplicate for 1–2 h. Each well then received 50 µL assay buffer and 10 µL DPP-IV enzyme, followed by 10 µL of inhibitor or vehicle. The reaction was initiated with 50 µL of H-Gly-Pro-p-nitroanilide and incubated for 30–60 min at 37 °C, and the absorbance of released p-nitroaniline was read at 405 nm [29,30].

Cell-based assay. L6 and 3T3-L1 cells were cultured in DMEM with 10% fetal bovine serum and 1% antibiotics at 37 °C in 5% CO_2 and used at 70–80% confluence. Phloridzin was dissolved in dimethyl sulfoxide and diluted in culture medium to 0.5, 1.0, 1.5, 2.0 and 2.5 µM, with sitagliptin prepared at equivalent concentrations as positive control; the final dimethyl sulfoxide concentration did not exceed 0.1% (v/v). Three treatment groups were studied in each cell line (Table 2). After 24 h of treatment, cells were washed with ice-cold phosphate-buffered saline, lysed in RIPA buffer on ice for 30 min and centrifuged at 12,000 rpm for 15 min at 4 °C, and the supernatant was taken as the enzyme source for the chromogenic assay described above.

Table 2. Treatment groups for the DPP-IV inhibition assay, applied identically in L6 and 3T3-L1 cells.

Group	Treatment	Concentrations (µM)
I	Control (untreated cells)	—

II	Phloridzin	0.5, 1.0, 1.5, 2.0, 2.5
III	Sitagliptin (reference inhibitor)	0.5, 1.0, 1.5, 2.0, 2.5

Inhibition was calculated as:

% DPP-IV inhibition = $[(A_{control} - A_{treated}) / A_{control}] \times 100$

2.10 Data handling and statistics

Values are expressed as mean ± standard deviation of triplicate determinations.

3. RESULTS

3.1 Molecular docking

Table 3 reports the Glide XP docking results for the five highest-ranked natural compounds alongside the redocked co-crystal ligand. Phloridzin achieved the most favorable g-score at −9.821 kcal/mol, followed by procyanidin (−9.466 kcal/mol) and mangiferin (−9.464 kcal/mol); all three scored better than the co-crystallized ligand (−8.384 kcal/mol). Magnolol (−8.177 kcal/mol) was comparable to the reference, and osthole was the weakest of the series (−4.527 kcal/mol).

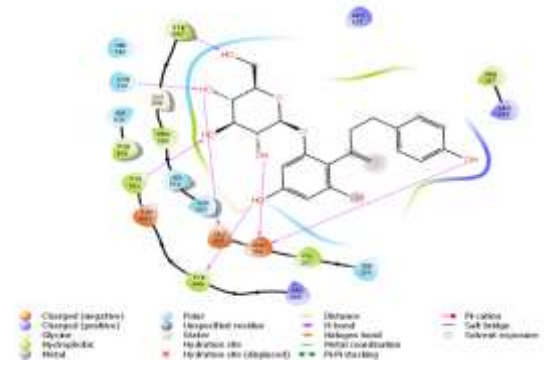
The hydrogen-bonding term separated the series more sharply than the total score. XP HBond values were −5.201 kcal/mol for phloridzin, −4.215 for procyanidin and −2.880 for mangiferin, against −0.773 for magnolol, −0.302 for osthole and −0.289 for the co-crystal ligand. This ordering tracks the polyhydroxylated character of the three leading compounds. The van der Waals term ordered the series differently: procyanidin, the largest ligand of the set, recorded the most favorable Glide evdw term (−41.236 kcal/mol), ahead of the co-crystal ligand (−35.468 kcal/mol) and well ahead of phloridzin (−20.808 kcal/mol). The total Glide energy was most favorable for the co-crystal ligand (−79.781 kcal/mol), followed by procyanidin (−54.529), phloridzin (−50.383), mangiferin (−42.770), magnolol (−31.944) and osthole (−27.719 kcal/mol). Phloridzin therefore ranks first on the scoring function used for selection while not dominating every individual energy term, a qualification carried forward into the Discussion.

Table 3. Glide extra-precision docking scores of the five highest-ranked natural compounds and the redocked co-crystal ligand in the DPP-IV active site (PDB ID: 2P8S). All values in kcal/mol.

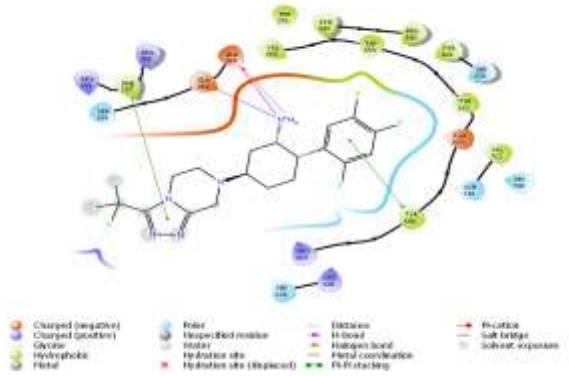
PubChem ID	Compound	Glide g-score	XP HBond	Glide evdw	Glide energy
6072	Phloridzin	−9.821	−5.201	−20.808	−50.383
107876	Procyanidin	−9.466	−4.215	−41.236	−54.529
5281647	Mangiferin	−9.464	−2.880	−25.304	−42.770
72300	Magnolol	−8.177	−0.773	−25.761	−31.944
10228	Osthole	−4.527	−0.302	−25.609	−27.719
417	Co-crystal ligand (417 cyclohexylamine)	−8.384	−0.289	−35.468	−79.781

Figure 2 shows the two-dimensional interaction diagrams for phloridzin and the co-crystal ligand. Phloridzin formed an extensive hydrogen-bonding network through its phenolic and sugar hydroxyl groups, engaging Asn710, Glu205, Glu206, Tyr662 and Tyr666 through the sugar moiety and Glu206 through the terminal phenol. The sugar hydroxymethyl group was oriented towards Tyr547, with additional polar and hydrophobic contacts to Ser630, Tyr631, Pro550, Gly549, Ser552, Gln553, Val207, Ser209, Arg125, Phe357, Arg358 and Arg669. Glu205 and Glu206 constitute the canonical glutamate motif of the DPP-IV S2 subsite [2], and both were substantially engaged.

The co-crystal ligand was anchored principally through its protonated primary amine, which formed a hydrogen bond and salt bridge with Glu205 and Glu206, together with π–π stacking to Tyr666 via the trifluorophenyl ring and to Phe357 via the triazolone linker. It occupied the same polar and hydrophobic envelope, contacting Trp201, Tyr547, Val656, Trp659, Tyr662, Val711, Ser209, Arg125, Arg356, Arg358 and Arg669. The two ligands thus exploit the same subsite by different means: a charge-anchored, stacking-dominated mode for the reference inhibitor, and a hydrogen-bond-dominated mode for the dihydrochalcone.



(A)



(B)

Figure 2. Two-dimensional protein–ligand interaction diagrams. (A) Phloridzin in complex with DPP-IV; (B) co-crystal ligand 417 cyclohexylamine in complex with DPP-IV (PDB ID: 2P8S).

3.2 MM-GBSA rescoring

MM-GBSA rescoring preserved the docking rank order at the top of the series (Table 4). Phloridzin returned the most favorable ΔG_{bind} at −79.494 kcal/mol, ahead of procyanidin (−61.575) and mangiferin (−41.815 kcal/mol), all three substantially more favorable than the co-crystal ligand (−20.289 kcal/mol).

The component terms clarify the origin of these differences. Phloridzin was dominated by an exceptionally favorable Coulombic term (−100.76 kcal/mol) with supporting hydrogen-bond (−5.573), lipophilic (−28.810) and van der Waals (−33.479 kcal/mol) contributions, consistent with the hydrogen-bonding and electrostatic engagement of Glu205 and Glu206 seen in the docked pose; these were sufficient to offset an unfavorable covalent strain term of 9.598 kcal/mol. Procyanidin drew more evenly on Coulombic (−30.924), van der Waals (−35.706), lipophilic (−22.111) and hydrogen-bond (−3.866 kcal/mol) terms. Mangiferin was driven mainly by van der Waals contact, recording the most favorable such term in the series (−41.677 kcal/mol) together with a lipophilic contribution of −24.033 kcal/mol, but a weak Coulombic term (−3.932) and a markedly unfavorable covalent term (21.634 kcal/mol) eroded its overall ranking. Magnolol carried an unfavorable Coulombic term (7.185 kcal/mol) with weak hydrogen-bond (−2.685) and van der Waals (−14.936 kcal/mol) contributions, and osthole was stabilized by Coulombic (−17.940), lipophilic (−22.035) and van der Waals (−22.813 kcal/mol) terms with

no net hydrogen-bond contribution (0.148 kcal/mol). The co-crystal ligand showed favorable Coulombic (−38.550) and covalent (−20.551 kcal/mol) terms consistent with its salt-bridge anchoring at Glu205 and Glu206, but these were largely cancelled by unfavorable hydrogen-bond (4.044), lipophilic (4.964) and van der Waals (2.415 kcal/mol) terms, giving a moderate overall ΔG_{bind}.

Table 4. Prime MM-GBSA binding free energies and component terms for the XP-docked complexes. All values in kcal/mol.

PubChem ID	Compound	ΔG_{bind}	$\Delta G_{coulomb}$	$\Delta G_{covalent}$	$\Delta G_{H\text{-}bond}$	ΔG_{lipo}	ΔG_{vdW}
6072	Phloridzin	−79.494	−100.76	9.598	−5.573	−28.810	−33.479
107876	Procyanidin	−61.575	−30.924	−3.868	−3.866	−22.111	−35.706
5281647	Mangiferin	−41.815	−3.932	21.634	−4.666	−24.033	−41.677
72300	Magnolol	−13.469	7.185	4.372	−2.685	−17.832	−14.936
10228	Osthole	−24.367	−17.940	−2.862	0.148	−22.035	−22.813
417	Co-crystal ligand	−20.289	−38.550	−20.551	4.0443	4.9638	2.415

3.3 Conformational stability of the phloridzin complex

Over the 100 ns trajectory the protein backbone was stable. The Cα RMSD remained between approximately 1.5 and 2.5 Å with a mean near 2.0 Å and no drift (Figure 3, left axis), indicating that the receptor fold was maintained throughout.

The ligand behaved differently, and the distinction matters. Referenced to the protein frame, the phloridzin RMSD rose from approximately 1.5 Å during the first 15 ns, climbed through a transition between roughly 15 and 25 ns, and thereafter oscillated between approximately 7 and 9.5 Å with excursions to about 10.5 Å for the remaining 75 ns (Figure 3, right axis). A plateau of this magnitude is not consistent with retention of the docked pose; it indicates that the ligand reorganized within the binding site early in the simulation and then settled into a different arrangement that was itself stable for the remainder of the run. The contact data in Section 3.4 support this reading, since the long-lived interactions of the trajectory are not identical to those of the docked pose.

Per-residue fluctuation was low across the structure and lowest where it matters (Figure 4). Most residues fluctuated between approximately 0.5 and 1.5 Å, with mobility concentrated in surface loops that peaked near 3.1 Å around residues 205–215 and near 2.8 Å around residue 500. Residues in contact with the ligand, marked on the figure, fluctuated below approximately 1 Å throughout, indicating that the binding site itself remained well ordered even as the ligand rearranged within it.

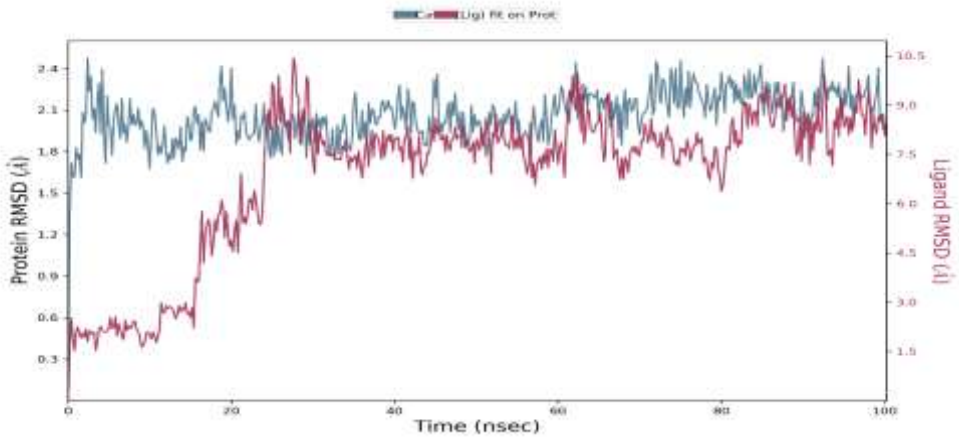


Figure 3. Protein and ligand RMSD for the phloridzin/2P8S complex over a 100 ns molecular dynamics simulation. Left axis, protein Cα RMSD (blue); right axis, ligand RMSD fitted on the protein (red). Note the difference in axis scales.

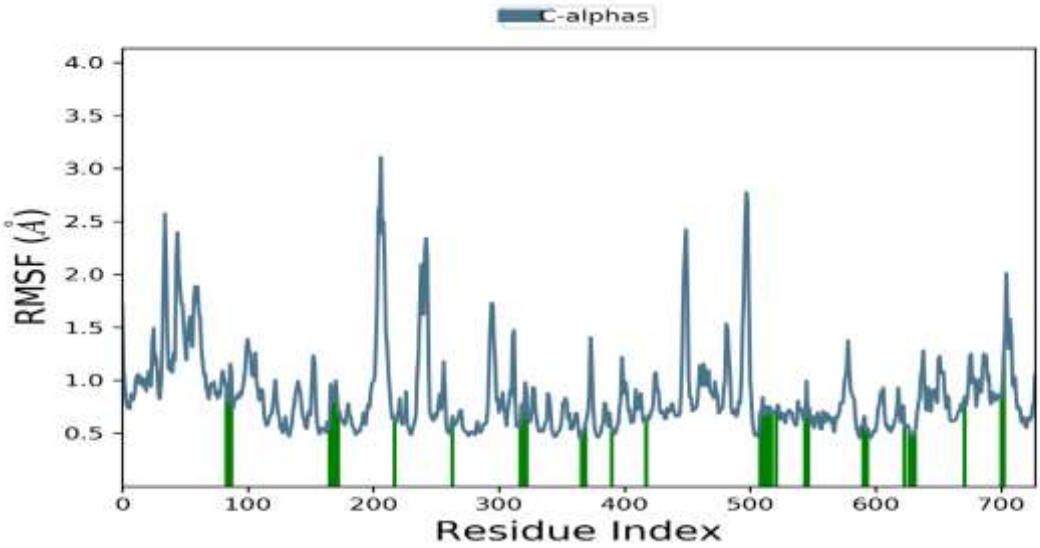


Figure 4. Per-residue root mean square fluctuation of protein Cα atoms over the 100 ns simulation. Vertical bars mark residues in contact with the ligand.

3.4 Protein–ligand contacts over the trajectory

The contact profile is shown in Figure 5. Interactions were distributed over Glu205, Glu206, Val207, Ser209, Phe357, Arg358, Arg429, Tyr456, Tyr547, Pro550, Cys551, Gln553, Asp556, Arg560, Tyr585, Ser630, Tyr662 and Tyr666, comprising hydrogen bonds, hydrophobic contacts, ionic interactions and water bridges. Glu205 dominated the profile with a total interaction fraction of approximately 1.76, a value exceeding unity because the residue sustains more than one contact of a given type simultaneously; its contribution was principally hydrogen bonding with additional ionic and water-bridged character. Glu206 (0.79), Asp556 (0.61), Ser209 (0.56), Tyr547 (0.47), Tyr585 (0.38) and Arg358 (0.32) followed, all values approximate. On the basis of contact persistence, Glu205, Ser209, Tyr547, Asp556 and Tyr585 are the residues occupied for the greatest fraction of the trajectory.

The specific hydrogen bonds carrying the complex are resolved in Figure 7. Two hydrogen bonds from the glucose moiety to Glu205 were present for 50% and 35% of the trajectory respectively, and a third from the terminal phenolic hydroxyl of the B-ring to Asp556 was present for 46%. An intramolecular hydrogen bond between the carbonyl oxygen and the adjacent 2'-hydroxyl was maintained for 63% of the trajectory, consistent with the intramolecular hydrogen bond count of 0 to 2 recorded in the ligand descriptors. Notably, Asp556 does not feature in the docked-pose interaction set of Section 3.1 but is among the most persistent contacts in the simulation, which is direct evidence for the pose rearrangement inferred from the ligand RMSD.

The persistence of these contacts through time is shown in Figure 6. Contact with the S2 glutamates is established early and is maintained in a broadly continuous band for the full trajectory, whereas several peripheral contacts appear only after the first 20–25 ns. This timing coincides with the ligand RMSD transition of Figure 3 and provides an independent view of the same event: the interaction set in place after 25 ns is not the one present at the start of the run.

Natural Resources for Human Health
eISSN: 2583-1194

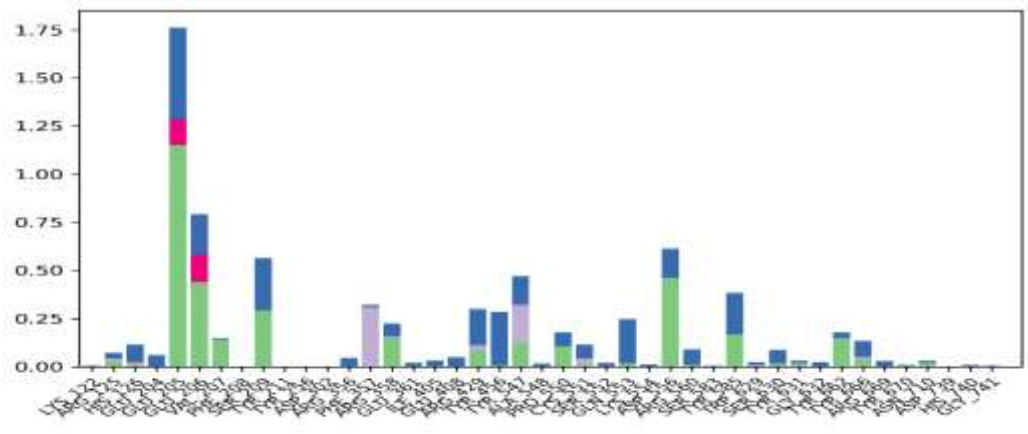


Figure 5. Protein–ligand contact profile for the phloridzin/2P8S complex over the 100 ns simulation, expressed as interaction fraction by residue. Contact types are stacked: hydrogen bonds (green), hydrophobic contacts (purple), ionic interactions (magenta) and water bridges (blue). Values above 1.0 indicate that a residue sustains more than one contact of a given type simultaneously.

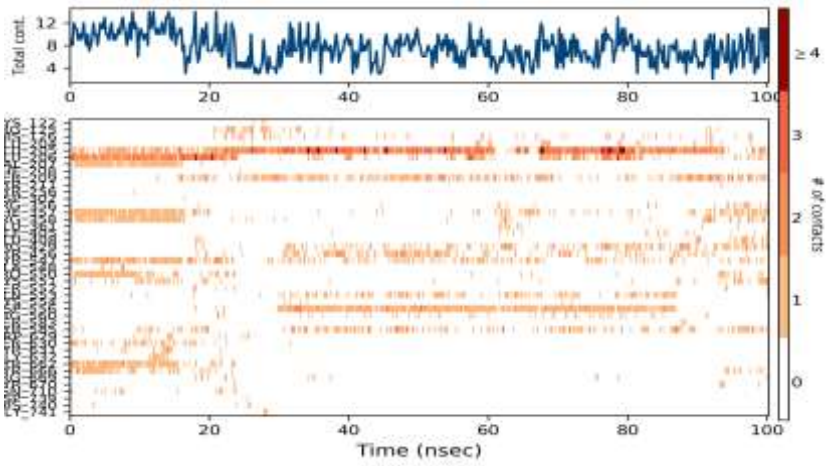


Figure 6. Timeline of protein–ligand contacts for the phloridzin/2P8S complex over the 100 ns simulation. The upper panel gives the total number of contacts through time; the lower panel resolves which residues are in contact at each frame, with darker shading indicating more contacts with that residue.

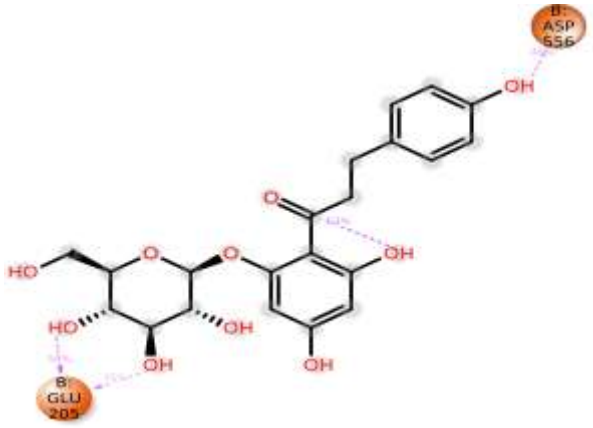


Figure 7. Schematic of the hydrogen bonds formed by phloridzin during the 100 ns simulation, with occupancies expressed as the percentage of the trajectory for which each interaction is present.

Ligand descriptors over the trajectory are given in Figure 8. The ligand RMSD computed against its own initial conformation remained between 1 and 3 Å, indicating that the internal geometry of phloridzin was essentially preserved and that the large protein-referenced RMSD reflects repositioning rather than distortion. The radius of gyration remained between 3.6 and 4.4 Å, intramolecular hydrogen bonds between 0 and 2, molecular surface area between 340 and 380 Å², solvent-accessible surface area between 200 and 400 Å², and polar surface area between 300 and 360 Å².

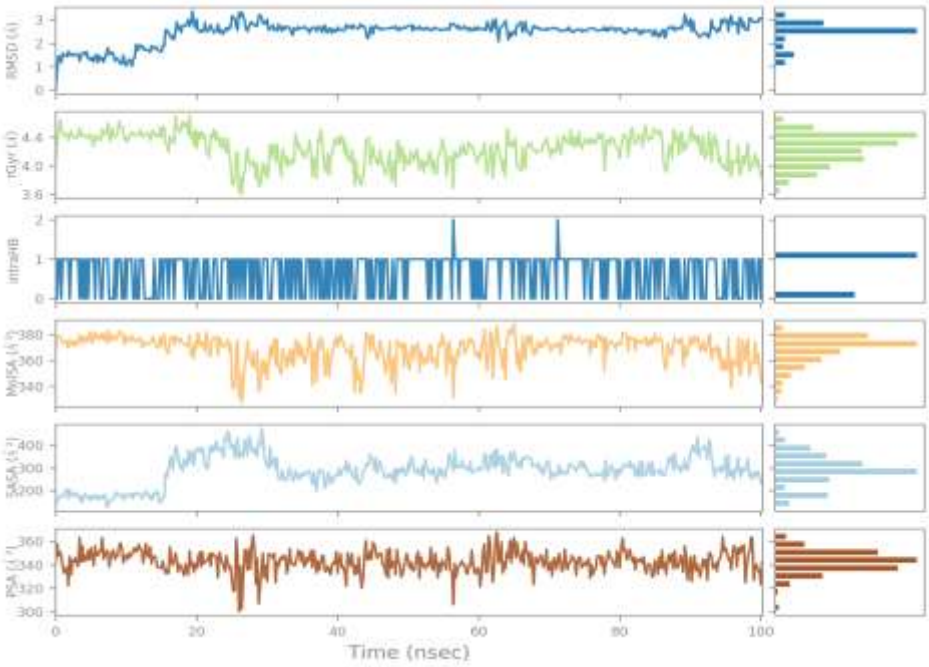


Figure 8. Ligand property descriptors for phloridzin over the 100 ns simulation: RMSD, radius of gyration (rGyr), intramolecular hydrogen bonds (intraHB), molecular surface area (MolSA), solvent-accessible surface area (SASA) and polar surface area (PSA).

3.5 DPP-IV inhibition in cells

Phloridzin inhibited DPP-IV in a concentration-dependent manner in both cell lines (Table 5, Figure 9). In L6 cells, inhibition rose from 11.61 ± 0.99% at 0.5 μM to 70.41 ± 0.74% at 2.5 μM, against 20.22 ± 1.12% to 72.28 ± 2.45% for sitagliptin over the same range. In 3T3-L1 cells, phloridzin produced 12.26 ± 2.51% inhibition at 0.5 μM rising to 74.71 ± 1.75% at 2.5 μM, against 18.00 ± 2.13% to 78.16 ± 1.41% for sitagliptin. Phloridzin was less potent than sitagliptin at every concentration tested in both systems.

The size of that difference was not, however, constant across the range (Figure 10). In L6 cells the shortfall relative to sitagliptin was 8.6 percentage points at 0.5 μM, rose irregularly to a maximum of 21.0 percentage points at 2.0 μM, then fell to 1.9 percentage points at 2.5 μM. In 3T3-L1 cells the same pattern occurred over a narrower span, with 5.7 percentage points at 0.5 μM, a maximum of 8.0 percentage points at 2.0 μM and 3.5 percentage points at 2.5 μM. This non-monotonic behavior reflects the steepness of the phloridzin response at the top of the range: between 2.0 and 2.5 μM phloridzin gained 24.7 percentage points of inhibition in L6 cells while sitagliptin gained only 5.6. The apparent near-equivalence of the two compounds at 2.5 μM therefore rests on a single steep interval at the upper limit of the concentrations tested and should not be over-interpreted; extending the range above 2.5 μM would establish whether the phloridzin curve genuinely converges on that of sitagliptin or merely crosses a steep segment.

Natural Resources for Human Health
eISSN: 2583-1194

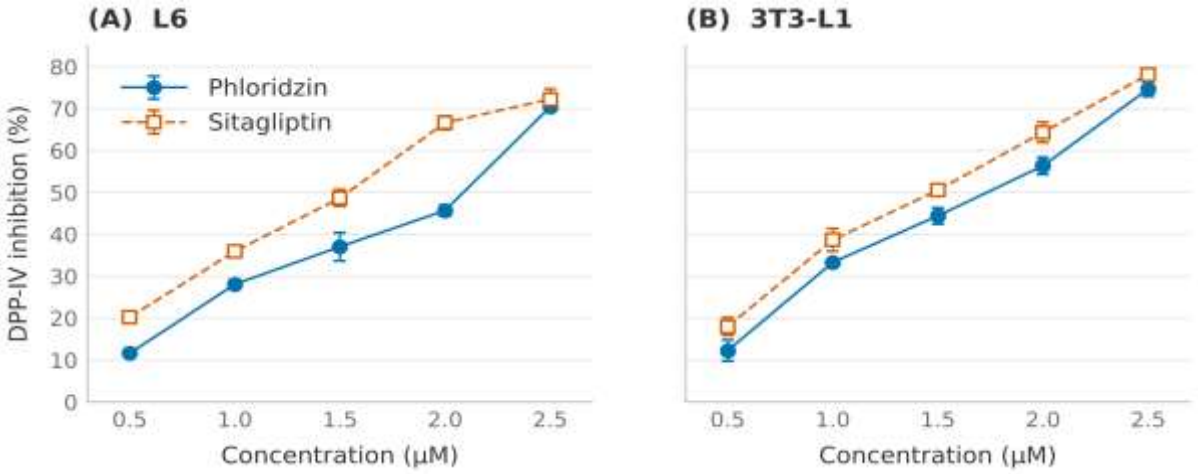


Figure 9. Concentration–response relationships for DPP-IV inhibition by phloridzin and sitagliptin in (A) L6 and (B) 3T3-L1 cells. Points are mean ± SD (n = 3) and are joined by straight segments; no curve has been fitted to the data. Plotted from the data in Table 5.

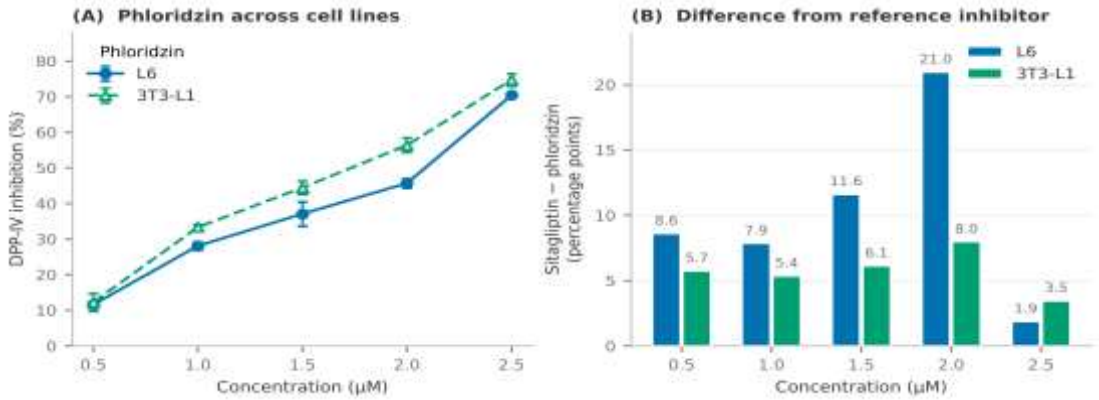


Figure 10. (A) Phloridzin DPP-IV inhibition compared between L6 and 3T3-L1 cells; points are mean ± SD (n = 3). (B) Difference between sitagliptin and phloridzin inhibition at each concentration, in percentage points, showing that the shortfall peaks at 2.0 μM in both cell lines rather than narrowing monotonically. Plotted from the data in Table 5.

Table 5. DPP-IV inhibition by phloridzin and sitagliptin in L6 and 3T3-L1 cells. Values are mean ± SD (n = 3).

Concentration (μM)	L6: phloridzin (%)	L6: sitagliptin (%)	3T3-L1: phloridzin (%)	3T3-L1: sitagliptin (%)
0.5	11.61 ± 0.99	20.22 ± 1.12	12.26 ± 2.51	18.00 ± 2.13
1.0	28.09 ± 1.12	35.95 ± 1.29	33.33 ± 0.66	38.69 ± 2.68
1.5	37.07 ± 3.37	48.68 ± 1.98	44.44 ± 1.91	50.57 ± 1.32
2.0	45.69 ± 1.35	66.66 ± 1.63	56.38 ± 2.02	64.36 ± 2.43
2.5	70.41 ± 0.74	72.28 ± 2.45	74.71 ± 1.75	78.16 ± 1.41

3.6 Glucose uptake

Phloridzin produced an increase in glucose uptake in both cell lines, measured as the difference between initial and final glucose content of the incubation medium against an insulin-treated reference.

4. DISCUSSION

This study set out to establish whether a structure-based prediction for a common dietary dihydrochalcone would be reproduced experimentally, and the two lines of evidence agree in direction. Phloridzin ranked first among the screened natural products on the Glide XP score and first again on MM-GBSA rescoring, in both cases ahead of the redocked sitagliptin analogue, and it went on to inhibit DPP-IV concentration-dependently in two cell lines, approaching sitagliptin at the top of the tested range. That convergence should be read cautiously, since it rests on a single steep interval between 2.0 and 2.5 μM rather than on a sustained narrowing of the difference across the range. The broader agreement is also worth stating carefully: docking scores are rank-ordering devices rather than affinity predictions, and the cellular assay is not a measure of the same quantity, so the appropriate claim is concordance of ranking rather than quantitative validation.

The structural basis of the interaction is the more informative result. Both phloridzin and the co-crystal ligand engage the glutamate pair Glu205/Glu206 that defines the S2 subsite of DPP-IV, but they do so by different chemistry. The reference inhibitor is anchored electrostatically through a protonated primary amine forming a salt bridge, supplemented by π-stacking at Tyr666 and Phe357- the canonical binding mode of the gliptin class. Phloridzin substitutes a dense hydrogen-bonding network supplied by its sugar and phenolic hydroxyls, which is reflected in its XP hydrogen-bonding term being an order of magnitude larger than that of the co-crystal ligand and in its very favorable MM-GBSA Coulombic component. The corollary is that phloridzin achieves a comparable rank through polar complementarity while recording a markedly weaker van der Waals term, indicating that it fills the hydrophobic envelope of the site less completely than either procyanidin or the reference ligand. For a medicinal chemist, that is an actionable observation: the dihydrochalcone scaffold presents an opportunity to retain the Glu205 anchor while adding hydrophobic bulk directed at the S1 pocket.

The molecular dynamics result requires an interpretation that differs from the one implied by docking alone. The protein was stable throughout, and the ligand-contacting residues were among the least mobile in the structure, so the binding site itself was well behaved. The ligand, however, departed from its docked pose during the first 25 ns and then held a distinct arrangement for the remaining 75 ns, as shown by a protein-referenced RMSD plateau at approximately 7–9.5 Å alongside an internal ligand RMSD that never exceeded 3 Å. The contact data corroborate this directly: Asp556 carries a hydrogen bond for 46% of the trajectory despite being absent from the docked-pose contact set, while the Glu205 hydrogen bonds persist at 50% and 35%. The most defensible reading is that phloridzin is retained in the active site - it does not dissociate, and the persistence of specific hydrogen bonds over tens of nanoseconds argues against non-specific association - but the pose that survives thermal motion is a rearranged one anchored at Glu205 and Asp556 rather than the pose selected by docking. This distinction has practical consequences, since structure-based optimization built on the docked pose alone would be optimizing the wrong geometry.

These findings sit alongside an independent computational study that docked phlorizin against the same DPP-IV structure and likewise found it to bind more strongly than sitagliptin, reporting −10.9 kcal/mol for phlorizin against −8.8 kcal/mol for the reference drug [11]. The convergence of two studies using different scoring functions on the same qualitative conclusion strengthens the case that the dihydrochalcone scaffold has genuine affinity for this site. The agreement is not complete, however, and the disagreement is instructive. That study reported phlorizin hydrogen bonding to Arg125, Asp545, Asp454, Gln553, Lys554 and Trp629 with hydrophobic and π-stacking contact at Tyr547, a contact set that overlaps the present docked pose only partially. The overlap is greater with the present simulation than with the present docked pose: Gln553 and Tyr547 appear in the trajectory contact profile, and the engagement of an aspartate residue is common to both accounts. Taken together, the two studies suggest that the docked pose of this flexible, highly hydroxylated ligand is poorly determined by scoring functions, and that simulation is necessary rather than confirmatory for ligands of this class.

The cellular data position phloridzin as a moderately potent inhibitor rather than a candidate to displace an optimized drug. Sitagliptin was more potent at every concentration in both cell lines, which is the expected result for a clinically optimized molecule compared with an unmodified natural product. The practical interest lies in the combination of appreciable activity at low micromolar concentrations with the wide dietary availability and documented tolerability of the parent compound. The use of two cell types with different metabolic identities - a skeletal muscle line and a preadipocyte line — provides a measure of generality, since DPP-IV is expressed in both muscle and adipose tissue and adipose-derived DPP-IV has been implicated in the metabolic consequences of obesity [1,6]. The concordance of the inhibition profiles between the two lines suggests that the effect is on the enzyme rather than on a cell-type-specific process.

4.1 Strengths and limitations

The principal strength of the study is the combination of an unbiased structure-based screen, a simulation long enough to reveal pose instability that docking could not, and experimental testing of the prioritized compound in two independent cell systems against a clinical reference inhibitor. The discrepancy between the docked and simulated poses is reported here rather than presented as a validated docking result.

Several limitations qualify the conclusions. First, docking scores and MM-GBSA energies are relative quantities computed on a rigid or near-rigid receptor and should not be read as affinities; the absolute values reported here carry no claim of thermodynamic accuracy. Second, no direct binding measurement was performed, so the molecular interaction inferred computationally is supported by functional enzyme inhibition but not by a biophysical affinity determination; surface plasmon resonance or isothermal titration calorimetry would be required to close that gap. Third, a single 100 ns trajectory without replicates cannot establish that the rearranged pose is the global free-energy minimum, and replicate simulations with independent velocity seeds, or enhanced-sampling free-energy methods, would be needed to characterize the rearrangement quantitatively. Fourth, no cytotoxicity endpoint is reported here, so the possibility that reduced cell number contributes to the apparent enzyme inhibition in the cell-based format cannot be formally excluded; the cell-free assay format is not subject to this concern. Fifth, the glucose-uptake observation is reported qualitatively only and is therefore not advanced as a quantitative finding. Sixth, the concentration range tested spans only five-fold and stops at 2.5 μM, which is close to the steepest part of the phloridzin response and leaves the upper plateau undefined; no half-maximal inhibitory concentration is therefore reported, and a wider range would be needed to characterize the curve properly. Seventh, selectivity was not assessed: DPP-IV belongs to a family that includes DPP-8 and DPP-9, combined inhibition of which produced severe toxicity in preclinical species and is the reason selectivity is now a standard requirement for this target class [31], and no counter-screen against these enzymes was performed. Finally, the study is confined to cell-based work; no animal data are reported here, and no claim about wound healing, formulation performance or in vivo efficacy is made or implied by these results.

4.2 Future directions

The immediate priorities follow from the limitations. Direct binding measurement would convert the computational inference into a measured affinity. Counter-screening against DPP-8 and DPP-9 would establish whether the polar binding mode confers selectivity [31], which is a plausible hypothesis given that the dihydrochalcone engages the S2 glutamates through hydrogen bonding rather than through the charged amine used by the gliptins. Replicate and enhanced-sampling simulations would characterize the pose rearrangement properly and could yield a better starting geometry for analogue design. Beyond the enzyme itself, the documented role of DPP-IV in the processing of SDF-1 and IGF-1 and in endothelial inflammation [1,3–6] offers a rationale for examining phloridzin in models of impaired tissue repair, and the delivery of such a compound to a wound bed from a hydrated polymer matrix is an established formulation strategy [32–35]. Those directions are stated here as prospective work; the present study provides no data on them.

5. CONCLUSION

Structure-based screening of a natural-product library against DPP-IV identified phloridzin as the highest-ranked candidate by both Glide XP docking and MM-GBSA rescoring, placing it ahead of the co-crystallized sitagliptin analogue in each case, with its advantage arising from an extensive hydrogen-bonding and electrostatic engagement of the Glu205/Glu206 motif of the S2 subsite. A 100 ns simulation showed a stable receptor and a well-ordered binding site, but also showed that phloridzin leaves its docked pose within the first 25 ns and occupies a distinct, persistent pose anchored by hydrogen bonds to Glu205 and Asp556 for the remainder of the trajectory. Experimentally, phloridzin inhibited DPP-IV concentration-dependently in both L6 and 3T3-L1 cells, reaching 70.41 ± 0.74% and 74.71 ± 1.75% inhibition at 2.5 μM against 72.28 ± 2.45% and 78.16 ± 1.41% for sitagliptin, and increased glucose uptake in both lines. Phloridzin is therefore a genuine, if moderately potent, natural DPP-IV inhibitor, and the pose rearrangement identified here should inform any subsequent optimization of the dihydrochalcone scaffold.

Acknowledgements

The authors would like to acknowledge the support and facilities provided by their institution during the course of this research. The authors are also grateful to all individuals who contributed directly or indirectly to the successful completion of this study.

Author Contributions

Vaishnavi Munnangi: Conceptualization, Methodology, Investigation, Data Curation.

Patel Dhruv Jatinkumar: Investigation, Laboratory Analysis, Data Curation.

Krishna Shevate and Kalirajan Rajagopal: Computational Analysis, Visualization, Validation.

Vadivelan Ramachandran: Supervision, Formal Analysis, Writing-Review & Editing.

Conflict of Interest

The authors declare that they have no competing interests related to this study.

Ethics Statement

Ethical approval was not required for the work described, subject to the applicable institutional guidelines.

Data Availability Statement

The data supporting the findings of this study are available within the article.

REFERENCES

[1] Röhrborn D, Wronkowitz N, Eckel J. DPP4 in diabetes. Front Immunol. 2015;6:386. doi:10.3389/fimmu.2015.00386
[2] Rasmussen HB, Branner S, Wiberg FC, Wagtmann N. Crystal structure of human dipeptidyl peptidase IV/CD26 in complex with a substrate analog. Nat Struct Biol. 2003;10(1):19–25. doi:10.1038/nsb882
[3] Suh DY, Hunt TK, Spencer EM. Insulin-like growth factor-I reverses the impairment of wound healing induced by corticosteroids in rats. Endocrinology. 1992;131(5):2399–403. doi:10.1210/endo.131.5.1425438
[4] Pala L, Rotella CM. The role of DPP4 activity in cardiovascular districts: in vivo and in vitro evidence. J Diabetes Res. 2013;2013:590456. doi:10.1155/2013/590456
[5] Ishibashi Y, Matsui T, Maeda S, Higashimoto Y, Yamagishi S. Advanced glycation end products evoke endothelial cell damage by stimulating soluble dipeptidyl peptidase-4 production and its interaction with mannose 6-phosphate/insulin-like growth factor II receptor. Cardiovasc Diabetol. 2013;12(1):125. doi:10.1186/1475-2840-12-125
[6] Bouchard L, Faucher G, Tchernof A, Deshaies Y, Lebel S, Hould FS, et al. Comprehensive genetic analysis of the dipeptidyl peptidase-4 gene and cardiovascular disease risk factors in obese individuals. Acta Diabetol. 2009;46(1):13–21. doi:10.1007/s00592-008-0049-4
[7] Werner S, Grose R. Regulation of wound healing by growth factors and cytokines. Physiol Rev. 2003;83(3):835–70. doi:10.1152/physrev.2003.83.3.835
[8] Armstrong DG, Boulton AJM, Bus SA. Diabetic foot ulcers and their recurrence. N Engl J Med. 2017;376(24):2367–75. doi:10.1056/NEJMra1615439
[9] Mutluoglu M, Uzun G, Turhan V, Gorenek L, Ay H, Lipsky BA. How reliable are cultures of specimens from superficial swabs compared with those of deep tissue in patients with diabetic foot ulcers? J Diabetes Complications. 2012;26(3):225–9. doi:10.1016/j.jdiacomp.2012.03.015
[10] Tian L, Cao J, Zhao T, Liu Y, Khan A, Cheng G. The bioavailability, extraction, biosynthesis and distribution of natural dihydrochalcone: phloridzin. Int J Mol Sci. 2021;22(2):962. doi:10.3390/ijms22020962
[11] Zabidi NA, Ishak NA, Hamid M, Ashari SE, Mohammad Latif MA. Inhibitory evaluation of Curculigo latifolia on α-glucosidase, DPP (IV) and in vitro studies in antidiabetic with molecular docking relevance to type 2 diabetes mellitus. J Enzyme Inhib Med Chem. 2021;36(1):109–21. doi:10.1080/14756366.2020.1844680
[12] Huang PK, Lin SR, Chang CH, Tsai MJ, Lee DN, Weng CF. Natural phenolic compounds potentiate hypoglycemia via inhibition of dipeptidyl peptidase IV. Sci Rep. 2019;9(1):15585. doi:10.1038/s41598-019-52088-7

[13] RCSB Protein Data Bank. Entry 2P8S: crystal structure of human dipeptidyl peptidase IV in complex with a sitagliptin analogue. doi:10.2210/pdb2P8S/pdb
[14] Malakar V, Dhanabal SP, Gowramma B, Jangra A, Kant K, El-Serehy HA, et al. Deciphering potent protein tyrosine phosphatase-1B inhibitors through in silico molecular docking, MMGBSA, and molecular dynamics. ChemistrySelect. 2025;10(4):e202403082. doi:10.1002/slct.202403082
[15] Sorokina M, Merseburger P, Rajan K, Yirik MA, Steinbeck C. COCONUT online: collection of open natural products database. J Cheminform. 2021;13(1):2. doi:10.1186/s13321-020-00478-9
[16] Asgaonkar K, Patil S, Daga Y, Gupta M, Sagar A, Shevate K, et al. In silico exploration of phytochemical based thiazolidinone-caffeic acid-indole new chemical entities for simultaneous management of diabetes and hypertension – a fascinating study. Cardiovasc Hematol Disord Drug Targets. 2023;23(1):21–30. doi:10.2174/1871529X23666230414084918
[17] Shevate K, Rajagopal K, Byran G, Mandala S, Antony J, Gurunathan M. Computational design of pyrrolo[2,1-f]triazine-based dual wild-type/mutant EGFR inhibitors: pharmacophore modelling, 3D-QSAR, quantum chemistry, and post-MD studies for breast cancer therapeutics. Pept Sci. 2025;117(6):e70012. doi:10.1002/pep2.70012
[18] Friesner RA, Murphy RB, Repasky MP, Frye LL, Greenwood JR, Halgren TA, et al. Extra precision Glide: docking and scoring incorporating a model of hydrophobic enclosure for protein-ligand complexes. J Med Chem. 2006;49(21):6177–96. doi:10.1021/jm051256o
[19] Lu C, Wu C, Ghoreishi D, Chen W, Wang L, Damm W, et al. OPLS4: improving force field accuracy on challenging regimes of chemical space. J Chem Theory Comput. 2021;17(7):4291–300. doi:10.1021/acs.jctc.1c00302
[20] Pandi AV, Malakar V, Jeyabalan JB, Sanjai M, Shevate K, Rajagopal K, et al. Integrated computational-based design of putative dual TrkA/TrkB agonists for Alzheimer's disease: pharmacophore modelling, docking, MM/GBSA, DFT and dynamics studies. Front Bioinform. 2026;6:1779769. doi:10.3389/fbinf.2026.1779769
[21] Li J, Abel R, Zhu K, Cao Y, Zhao S, Friesner RA. The VSGB 2.0 model: a next generation energy model for high resolution protein structure modeling. Proteins. 2011;79(10):2794–812. doi:10.1002/prot.23106
[22] Shevate K, Rajagopal K, Byran G, Unni A, Antony J. Targeting TNBC metastasis: in silico identification of natural origin ROCK inhibitors via virtual screening, ADMET profiling, MM-GBSA, DFT, and molecular dynamics. Comput Biol Chem. 2026;120:108671. doi:10.1016/j.compbiolchem.2025.108671
[23] Asgaonkar KD, Naik AP, Shah PA, Ghate DD, Kachare SS, Rathod GP, et al. Designing of pyrazole derivatives using 3D-QSAR, ADMET, molecular docking and MD simulations for enhanced antibacterial properties. Lett Org Chem. 2025;22(12):946–57. doi:10.2174/0115701786360412250709155912
[24] Arumugam M, Vijayan P, Raghu C, Ashok G, Dhanaraj SA, Kumarappan CT. Anti-adipogenic activity of Capsicum annum (Solanaceae) in 3T3 L1. J Complement Integr Med. 2008;5(1):Article 1151. doi:10.2202/1553-3840.1151
[25] Papazisis KT, Geromichalos GD, Dimitriadis KA, Kortsaris AH. Optimization of the sulforhodamine B colorimetric assay. J Immunol Methods. 1997;208(2):151–8. doi:10.1016/S0022-1759(97)00137-3
[26] Skehan P, Storeng R, Scudiero D, Monks A, McMahon J, Vistica D, et al. New colorimetric cytotoxicity assay for anticancer-drug screening. J Natl Cancer Inst. 1990;82(13):1107–12. doi:10.1093/jnci/82.13.1107
[27] Noipha K, Purintrapiban J, Herunsalee A, Ratanachaiyavong S. In vitro glucose uptake activity of Tinospora crispa in skeletal muscle cells. Asian Biomed. 2008;2:415–20.
[28] Vadivelan R, Dhanabal SP, Wadhawani A, Elango K. α-Glucosidase and α-amylase inhibitory activities of Raphanus sativus Linn. Int J Pharm Sci Res. 2012;3(9):3186–8.
[29] Al-Masri IM, Mohammad MK, Taha MO. Inhibition of dipeptidyl peptidase IV (DPP IV) is one of the mechanisms explaining the hypoglycemic effect of berberine. J Enzyme Inhib Med Chem. 2009;24(5):1061–6. doi:10.1080/14756360802610761
[30] Chakrabarti R, Singh B, Narendra P, Varghese N, Vanchhawng L, Kanwal A, et al. Dipeptidyl peptidase-IV inhibitory activity of Berberis aristata. J Nat Prod (India). 2011;4:158–63.
[31] Lankas GR, Leiting B, Roy RS, Eiermann GJ, Beconi MG, Biftu T, et al. Dipeptidyl peptidase IV inhibition for the treatment of type 2 diabetes: potential importance of selectivity over dipeptidyl peptidases 8 and 9. Diabetes. 2005;54(10):2988–94. doi:10.2337/diabetes.54.10.2988
[32] Li J, Yu F, Chen G, Liu J, Li XL, Cheng B, et al. Moist-retaining, self-recoverable, bioadhesive, and transparent in situ forming hydrogels to accelerate wound healing. ACS Appl Mater Interfaces. 2020;12(2):2023–38. doi:10.1021/acsami.9b17180

[33] Brumberg V, Astrelina T, Malivanova T, Samoilov A. Modern wound dressings: hydrogel dressings. Biomedicines. 2021;9(9):1235. doi:10.3390/biomedicines9091235

[34] Augustine R, Hasan A, Dalvi YB, Rehman SRU, Varghese R, Unni RN, et al. Growth factor loaded in situ photocrosslinkable poly(3-hydroxybutyrate-co-3-hydroxyvalerate)/gelatin methacryloyl hybrid patch for diabetic wound healing. Mater Sci Eng C. 2021;118:111519. doi:10.1016/j.msec.2020.111519

[35] Jeong S, Kim B, Park M, Ban E, Lee SH, Kim A. Improved diabetic wound healing by EGF encapsulation in gelatin-alginate coacervates. Pharmaceutics. 2020;12(4):334. doi:10.3390/pharmaceutics12040334